Narrow Rupture of the 2020 M_w 7.4 La Crucecita, Mexico, Earthquake

Rumeng Guo[1,2,3], Hongfeng Yang[1], Yifan Zhu[4], Yong Zheng[*5], Jianqiao Xu[2], Lupeng Zhang[6,7], and Chao An[4]

Abstract

On 23 June 2020, a large (M_w 7.4) interplate thrust earthquake struck near the town of La Crucecita in the state of Oaxaca in southern Mexico, following a 55-yr interseismic period. A seismic source model is well constrained by teleseismic waveforms, static Global Positioning System offsets, and tsunami data, suggesting that the earthquake occurred on the slab interface at a dip of ∼23°, with a narrow elliptical asperity concentrating around a shallow depth of ∼20 km. The rupture propagates bilaterally from the hypocenter, and the down-dip rupture is restricted to ∼25 km by slow slip events (SSEs). The down-dip shear stress is released by SSEs during the interseismic period, limiting the earthquake magnitude and possibly resulting in the characteristic earthquake. The 2020 La Crucecita event, thus, is a good reminder to assess the seismic and tsunami potential in this region. The stress changes caused by the coseismic slip of the 2017 M_w 8.2 Chiapas earthquake are too small to trigger the 2020 La Crucecita earthquake. However, combined with the postseismic afterslip effects that play a leading role, it greatly promotes the eventual occurrence of the La Crucecita event. The results demonstrate the importance of considering postseismic afterslip, when evaluating seismic hazard and its migratory pattern.

Cite this article as Guo, R., H. Yang, Y. Zhu, Y. Zheng, J. Xu, L. Zhang, and C. An (2021). Narrow Rupture of the 2020 M_w 7.4 La Crucecita, Mexico, Earthquake, *Seismol. Res. Lett.* **XX**, 1–9, doi: 10.1785/0220200328.

Supplemental Material

Introduction

The southern Mexican subduction zone (MSZ) of the Cocos plate beneath the North American plate is a seismically active region, where the relative convergence rate at the Oaxaca state is ∼70 mm/yr (Fig. 1; DeMets *et al.*, 2010). It is a natural laboratory for probing into different slip patterns due to the short offshore distance that brings broad segments of the seismogenic and transition zones together. This area has a well-defined short seismic recurrence of 30–50 yr and is noted for the frequent occurrence of large shallow interplate earthquakes (e.g., Singh *et al.*, 1981). However, the observed maximum seismogenic depth is ∼25 ± 5 km, which is only about half of that in the most subduction zones (Singh *et al.*, 1981; Tichelaar and Ruff, 1993; Suárez and Sánchez, 1996; Gao and Wang, 2017). The relatively shallow seismogenic depth may explain smaller thrust events along the middle American trench than what is expected for a young subduction zone with a rapid convergence rate. In fact, most of the largest Mexican earthquakes were of magnitude 7.5 (Singh *et al.*, 1981; Suárez and Sánchez, 1996). Instrument records show that the tsunamis generated by the Mexican subduction earthquakes are relatively small, although, some scholars have suggested that great tsunamis struck the Pacific coast of Mexico in the past (Ramírez-Herrera *et al.*, 2020). Moreover, slow slip events (SSEs) have often been observed in the MSZ (Correa-Mora *et al.*, 2009; Song *et al.*, 2009; Graham *et al.*, 2014, 2016; Obara and Kato, 2016; Fasola *et al.*, 2019; Cruz-Atienza *et al.*, 2020). These SSEs generally take place in the down-dip transition zone of the locked section, in which large thrust earthquakes occur (e.g., Song *et al.*, 2009; Obara and Kato, 2016).

On 23 June 2020 at 15:29:04 UTC, a large M_w 7.4 earthquake struck the Oaxaca coast of southern Mexico, causing strong shaking in nearby towns such as La Crucecita. The Mexican Servicio Sismológico Nacional (SSN) reported that the earthquake occurred on a west–northwest thrust fault with a hypocenter 22 km beneath 15.803° N, 96.134° W (see Data and Resources). The hypocenter (15.887° N, 96.006° W, 20 km deep; see Data and Resources) estimated by the U.S. Geological

1. Earth System Science Programme, The Chinese University of Hong Kong, Shatin, Hong Kong, China; 2. State Key Laboratory of Geodesy and Earth's Dynamic, Innovation Academy for Precision Measurement Science and Technology, Chinese Academy of Science, Wuhan, China; 3. College of Earth and Planetary Sciences, University of Chinese Academy of Sciences, Beijing, China; 4. Key Laboratory of Hydrodynamics (Ministry of Education), School of Naval Architecture, Ocean and Civil Engineering, Shanghai Jiao Tong University, Shanghai, China; 5. State Key Laboratory of Geological Processes and Mineral Resources, Institute of Geophysics and Geomatics, China University of Geosciences, Wuhan, China; 6. Faculty of Geosciences and Environmental Engineering, Southwest Jiaotong University, Chengdu, China; 7. Division of Geodetic Science, School of Earth Science, Ohio State University, Columbus, Ohio, U.S.A.

*Corresponding author: zhengyong@cug.edu.cn

Survey (USGS) National Earthquake Information Center (NEIC) is located about ~16 km northeast of the SSN location (Fig. S1, available in the supplemental material to this article). Such difference in locations between global and local catalogs is common for Mexican earthquakes (Hjörleifsdóttir *et al.*, 2016). A cross section of the source region in Figure S1 also shows that the hypocenters fetched from database of the GEOFON project (see Data and Resources) and the Japan Meteorological Agency (see Data and Resources). These solutions all suggest a relatively shallow nucleation depth.

The 2020 M_w 7.4 La Crucecita earthquake caused devastating shaking and landslides, with at least 10 fatalities and damage to 2000 homes (Tracy *et al.*, 2020). The Servicio Mareográfico Nacional of Mexico reported a moderate tsunami, and, the maximum variations were registered in the Salina Cruz (SALI) stations, with a maximum of 1.4 m and Huatulco (HUAT) with 0.6 m, with respect to the level of the tide. Several large interplate thrust events struck the coast of Oaxaca in the mid-to-late last century, including the 1965 M_w 7.5 east Oaxaca event, the 1968 M_w 7.3 west Oaxaca event, and the 1978 M_w 7.7 central Oaxaca event (Chael and Stewart, 1982; Universidad Nacional Autónoma de México (UNAM) Seismology Group, 2013). Rousset *et al.* (2016) suggested that the Oaxaca region has high interseismic coupling and great seismic risk. Interestingly, the 2018 M_w 7.2 Pinotepa earthquake occupied a large part of the aftershock region of the 1968 event, whereas the 2020 M_w 7.4 La Crucecita earthquake occurred within the aftershock area of the 1965 event (Melgar *et al.*, 2020). Therefore, the unruptured source region of the 1978 event may have a high seismic potential in the future (Fig. 1b). The La Crucecita event provides an opportunity to verify systematic slip pattern of the plate interface. It is of great significance for us to assess the seismic hazard and tsunami potential in the MSZ.

Here, we resolve the rupture process of the 2020 La Crucecita earthquake with the kinematic joint inversion method, using teleseismic body waves and static Global Positioning System (GPS) offsets. To assess the tsunami hazard of this event and verify the accuracy of the dislocation distribution, we simulate deep-water tsunami recordings. Finally, we discuss the possible relationship between the coseismic rupture termination of the La Crucecita event and the down-dip SSEs, and estimate the triggering potential from the 2017 M_w 8.2 Chiapas earthquake.

Data and Method

We select 42 *P* and 12 *SH* teleseismic waveforms with good azimuthal distribution and high signal-to-noise ratio (SNR) from the Incorporated Research Institutions for Seismology Data Management Center (Fig. 1; see Data and Resources). Their epicenter distances are in the range of 30°–90°, to avoid waveform complexities from crust and upper-mantle heterogeneities and the core–mantle boundary variations (Kumar *et al.*, 2017). Because *P* waves attenuate more slowly with distance than *SH* waves, and the first motion pick of *P* phases is easier than that of *SH* phases, we apply more *P* waves and set the weight of the *P* wave twice that of the *SH* wave to improve the reliability of the inversion. Each waveform is deconvolved to ground velocities at a sampling rate of 0.2 s, after removing instrument responses and band-pass filtered over the range of 0.002–0.5 Hz; a wide frequency range is used to retrieve the complicated rupture history. We calculate the teleseismic Green's functions using the generalized ray theory, and reflection and refraction coefficient method (Helmberger, 1974).

The static coseismic GPS offsets are available from the Nevada Geodetic Laboratory (Blewitt *et al*, 2018; see Data and Resources). We select five GPS stations (OAX2, OXPE, OXUM, TNNP, and TNSJ) with relatively large displacement signals to use in the joint inversion (Fig. 1). The station OXUM with the maximum coseismic displacement rose over 4 cm in vertical and moved over 16 cm in southwest, attesting that some significant deformation did occur below this GPS site (Fig. 2b). Each station has the same weight in the inversion. The static Green's functions are calculated by the generalized reflection–transmission coefficient matrix method (Xie and Yao, 1989).

This earthquake generated relatively small tsunami waves, which were recorded by the Deep-ocean Assessment and Reporting of Tsunamis (DART) buoy 43413 and two tide gauges HUAT and SALI (Fig. 1). The raw data at the DART station are downloaded from the National Oceanographic and Atmospheric Administration National Data Buoy Center, and the sea-level recordings at the tide gauges are collected from the Intergovernmental Oceanographic Commission (see Data and Resources). During the simulation, we adopt the half-space elastic model (Okada, 1985) to predict the static seafloor deformation from the finite-fault model. By assuming instantaneous rupture and incompressible water, the initial sea surface elevation is the summation of the ocean-bottom vertical displacement and the contribution of horizontal displacement (Tanioka and Satake, 1996; Hu *et al.*, 2020). We then use the linear version of COMCOT (Wang and Liu, 2007; An *et al.*, 2014), which solves the nonlinear shallow water equations, to simulate the propagation of tsunami waves. The General Bathymetric Chart of the Oceans (2020) bathymetry data, with a resolution of 15 arcsec, are used (see Data and Resources). The timestep is set as 0.8 s to satisfy the Courant–Friedrichs–Lewy condition, and the total simulation time is constrained to 12,000 s.

We jointly invert the coseismic static three-component GPS displacements and teleseismic body waves, using a simulated annealing method (Ji *et al.*, 2002). During the inversion, the weight of the GPS dataset is twice that of the teleseismic body wave, because the surrounding GPS data are sparse but sensitive to the fault geometry and slip details. This nonlinear inversion algorithm could simultaneously resolve the slip magnitude, rake angle, rise time, and rupture velocity for each subfaults

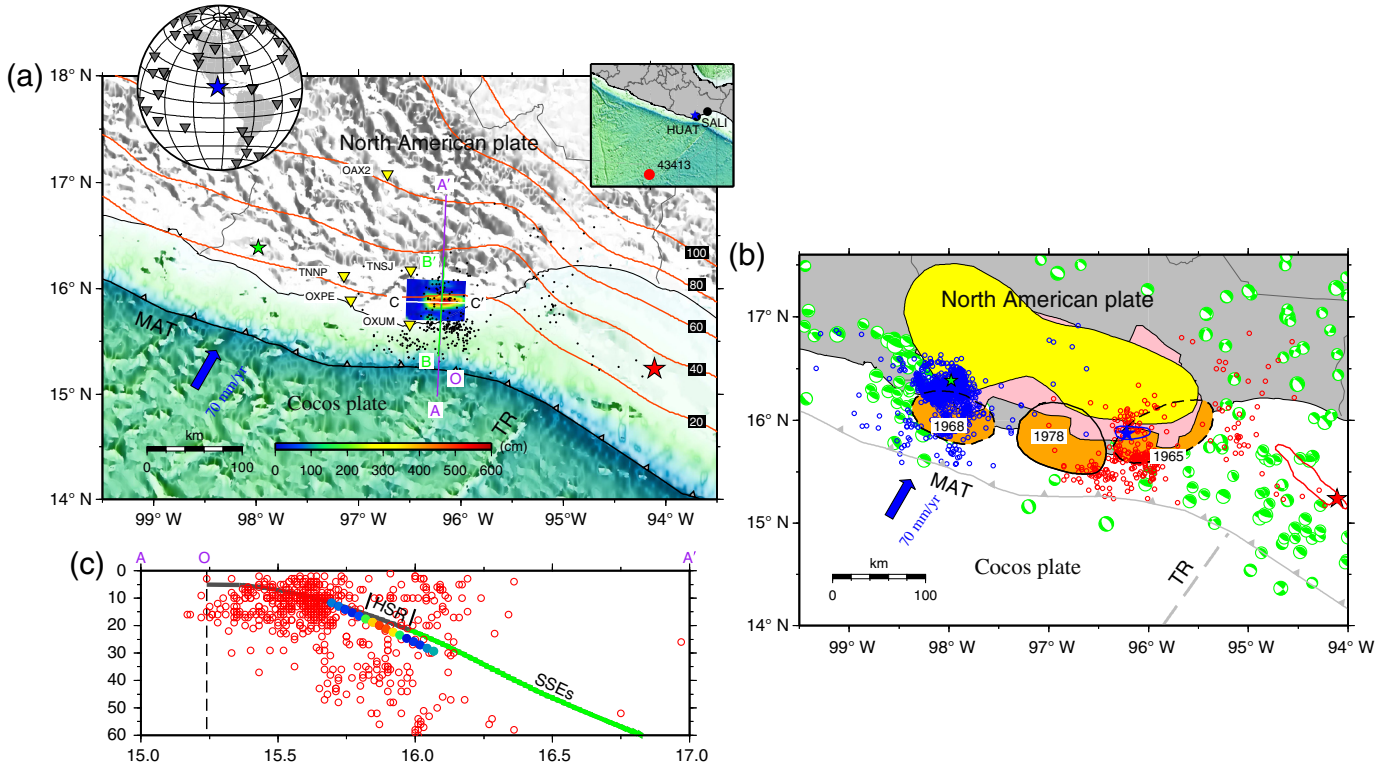

Figure 1. Tectonic background and seismicity around the 2020 La Crucecita earthquake. (a) Data coverage and slip model. The colored rectangle represents the surface projection of dislocation distribution for our preferred model. Black dots show the aftershocks within one week after the mainshock from Servicio Sismológico Nacional (SSN). Green, red, blue stars illustrate the epicenters of the 2018 M_w 7.2 Pinotepa event, the 2018 M_w 8.2 Chiapas event, and the 2020 M_w 7.4 La Crucecita event, respectively. The blue arrow represents the convergent rate (DeMets *et al.*, 2010). Orange contours illustrate slab surface depths with 20 km intervals from slab1.0 model (Hayes *et al.*, 2012). Yellow-inverted triangles represent Global Positioning System (GPS) stations. The inset panel in upper-left corner shows the distribution of teleseismic stations. The inset panel in upper-right corner shows the distribution of tide gauge (black points), and Deep-ocean Assessment and Reporting of Tsunamis (DART) (red point) stations. Profiles A–A′, B–B′, and C–C′ are described later. (b) Seismicity around the 2020 La Crucecita earthquake. Green focal mechanism plots are historical earthquakes between 1787 and 2018 from Sawires *et al.* (2019). Blue and red circles represent the one week aftershock sequences of the 2018 M_w 7.2 Pinotepa earthquake and the 2020 La Crucecita earthquake, respectively. Red and blue curves show the slip contour of 2 m for the 2017 Chiapas event from Guo *et al.* (2019) and the 2020 La Crucecita event from our preferred model, respectively. Orange-shaded regions are aftershock zones of historical earthquakes, and those surrounded by dashed lines are not well constrained (UNAM Seismology Group, 2013). Pink shadow depicts the slow slip events (SSEs) from October 2011 to March 2012, obtained by Graham *et al.* (2014). Yellow shadow illustrates the 1 cm aseismic slip contours imaged between September and December 2017 from Cruz-Atienza *et al.* (2020). (c) Depth profile of aftershock sequence (red circles), slip distribution (colored circles), and SSEs (green curve) along profile A–A′. The gray curve represents the slab surface along profile A–A′. HSR, high-slip region; MAT, Middle American trench; TR, Tehuantepec ridge.

(Ji *et al.*, 2002). The rake angle is allowed to vary between 0° and 140°; the maximum slip magnitude is set to 7 m; the rise time could vary from 0.6 to 7.0 s; the rupture velocity is constrained within the range of 0.5–4.0 km/s. To stabilize the inversion, two constraints are applied: one minimizes the total seismic moment (reference moment of 1.42×10^{20} N · m), and another one minimizes the differences between the slip on adjacent subfaults (Hartzell *et al.*, 1996; Ji *et al.*, 2002; Guo, Zheng, An, *et al.*, 2020).

Parameters Tests and Inversion Results

Ideally, we could explore the parameter space by analyzing possible combinations of different model parameters. We, thus, adopt a trial-and-error method to estimate model space associated with the epicenter location, fault geometry (strike and dip), and average rupture velocity (Fig. S2). The rupture initiation point may determine the magnitude of earthquake (Yang *et al.*, 2019) and significantly affect the results of finite-fault inversion (Chu *et al.*, 2011). Therefore, we conduct a series of preliminary finite-fault joint inversion to relocate the hypocenter location. The grid-search result shows an optimal nucleation point at 15.87° N, 96.22° W (Fig. S2a), which is located about 23 km west of the USGS location and 12 km northwest of the SSN location (Fig. S1a). The depth is difficult to constrain in the relocation, and we fix it at 20 km, same as

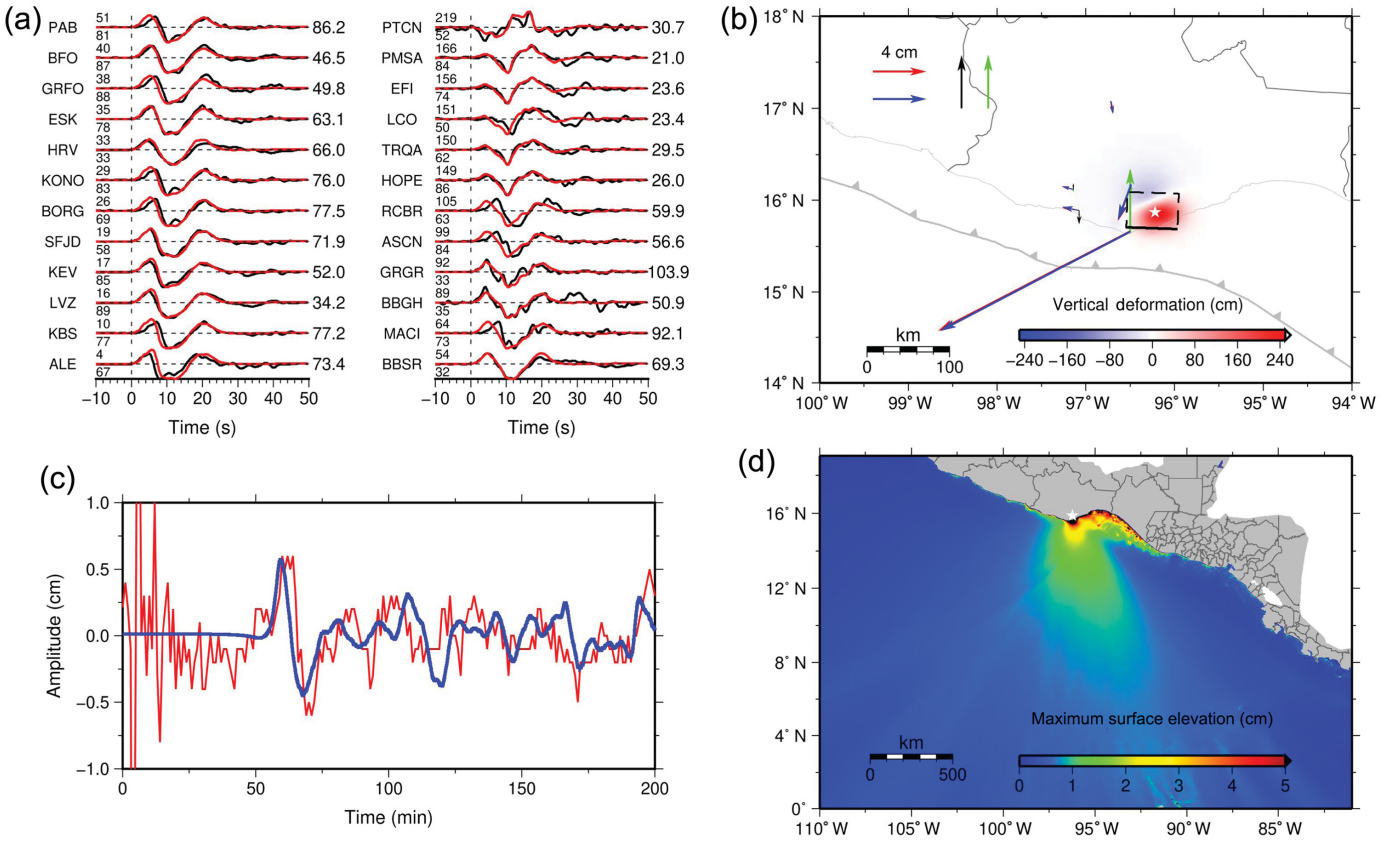

Figure 2. Comparison of observations and predictions for our preferred model. (a) Comparison of a subset of teleseismic velocities. Black and Red lines represent observed and predicted *P* waveforms, respectively. Both observations and predictions are aligned with the *P* arrivals. The station name is in the leftmost column of the record. The epicentral distance and azimuth (°) are illustrated at the beginning of each recording, with the azimuth at the top. The peak velocity in mm/s is stated at the end of each trace. Comparison of all additional observations and predictions is shown in Figure S4. (b) Comparison of static GPS offsets. Red and blue arrows show the observed and predicted horizontal GPS deformation, respectively. Black and green arrows show the observed and predicted vertical GPS deformation, respectively. Background color indicates predicted vertical deformation. (c) Comparison of observed (red line) and simulated (blue line) tsunami waves at the DART station 43413. (d) Maximum tsunami wave amplitude for the 2020 La Crucecita event. The white star is the event epicenter.

the NEIC solutions (Fig. S1b). Then, to completely determine the seismogenic fault location, we simultaneously retrieve the strike and dip. The optimal fault strike and dip are 272° and 23° (Fig. S2b), respectively, coinciding with the slab interface from slab1.0 model (Fig. 1c; Hayes *et al.*, 2012). The fault plane is discretized into 256 subfaults with dimensions of 4.0 km × 3.0 km. Finally, we systematically adjust the average rupture speed between 2.4 and 3.4 km/s, to achieve the optimal solution with the smallest misfit. As shown in Figure S2c, the preferred average rupture speed is 3.0 km/s, consistent with the result of Melgar *et al.* (2020). We also conduct an additional test by fixing the rupture initiation based on the SSN hypocenter, and then search for the optimal fault geometry. The results show that the misfit is the smallest when the strike and dip are 266° and 24°, respectively (Fig. S3a).

Figure 2a shows a subset of the teleseismic *P*-waveform fits for our preferred model, and additional comparisons are shown in Figure S4. Figure 2b illustrates the comparison of static horizontal and vertical GPS displacements. All offsets are well retrieved, except for the vertical components of stations OXPE and TNNP with low SNR. In addition, it can be observed that the fit of our preferred search model is significantly better than that of the model with a fixed hypocenter, especially for the near-field GPS data (Fig. S5). Figure 2c and Figure S6 show the observed and simulated tsunami recordings from DART and tide gauge stations, based on our preferred slip distribution, respectively. Although, this event results in weak tsunami signals, we obtain satisfactory predicted tsunami waves at the DART station 43413, where the leading crest and trough are well reproduced. At the tide gauge HUAT, the initial uplift signal due to seafloor deformation is well recovered, whereas our model gives a lower subsequent trough than observation (Fig. S6a). At SALI, both the leading crest and periods of trailing waves are recovered, although, the amplitude is underestimated (Fig. S6b). We infer that the amplitude of trailing waves can be better predicted with more accurate

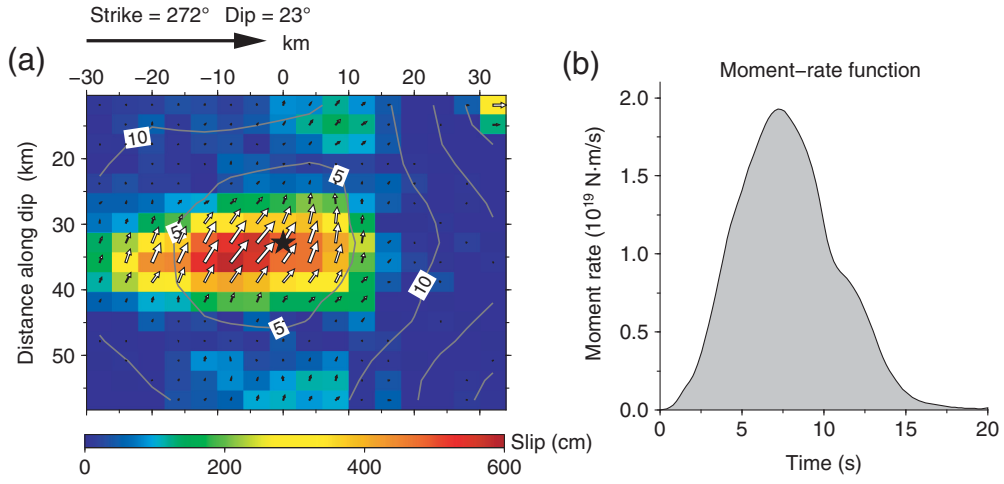

Figure 3. Our preferred rupture model for the 2020 La Crucecita earthquake. (a) Dislocation distribution. White arrows represent the rake angle of each subfault. The black star is the hypocenter, and gray curves represent the 5 s isochrones of the expanding rupture front. (b) Moment-rate function.

bathymetric data. The envelope of maximum surface elevation shows that the energy of tsunami waves propagates mainly in the northeast and southwest directions, nearly perpendicular to the trench (Fig. 2d). From the snapshots of our model (Fig. S7), the tsunami waves are trapped in the Tehuantepec shelf, causing the peak amplitude to increase to more than 0.1 m, which is much larger than that outside the shelf (less than 0.05 m). The coastal area around Huatulco that is directly influenced by the crustal deformation is struck by tsunami waves up to ~0.5 m, which can be seen directly in the tsunami recordings (Fig. S6a). In summary, the simulation of tsunami wave yields good fits to tsunami recordings, suggesting that the overall energy release and rupture dimension are well constrained in our model. Therefore, the slip distribution from our preferred model gives excellent fits to the seismic (Fig. 2a and Fig. S4) and geodetic (Fig. 2b) data and predicts the tsunami recordings (Fig. 2c and Fig. S6) well. Overall, this is an accurate and reliable rupture model.

The slip distribution in the model with a fixed hypocenter from the SSN catalog is illustrated in Figure S3b, including a small slip patch that may be unrealistic. Figure 3a shows our preferred rupture model. We find that the coseismic slip distribution is concentrated in a single asperity, rake angle variation of which is minor. The high-slip patch is well constrained in the depth range of 17–24 km, and the peak slip is 5.8 m at ~21 km depth (Fig. 1a). Compared with the results of Melgar *et al.* (2020), our preferred slip distribution is confined to a shallower and smaller elliptical asperity. The peak slip is greater than that of Melgar *et al.* (2020) but is still smaller than the rapid USGS solution (~8 m). No significant slip occurs at depths shallower than ~15 km (Fig. 1a), which is consistent with the moderate tsunami. There is also no significant slip extending into the deep ocean, consistent with the absence of the ringing coda wave in the *P* wavefield (*pwP*; Fig. S4; Lay and Rhode, 2019). The nucleation (hypocenter) initiates roughly at the center of the fault plane, and the rupture propagates bilaterally along strike. Large slip is found near the hypocenter (Fig. 3a), compatible with sharp onsets of teleseismic *P* waves (Fig. S4). Moreover, we model the coseismic vertical response of the Earth's crust to the La Crucecita event, based on the numerical code PSGRN & PSCMP (Wang *et al.*, 2006). The results illustrate that the maximum vertical deformation does occur near the epicenter (Fig. 2b).

Figure 3b shows that the rupture process lasts ~15 s, and the seismic moment reaches the peak value at 7.2 s. It illustrates a more symmetrical energy release pattern than the model of Melgar *et al.* (2020), whose results showed a more rapid moment rate, with a peak moment at ~5 s. Similar moment rate functions were also observed for the 2012 M_w 7.5 Ometepec earthquake and the 2018 M_w 7.2 Pinotepa earthquake in the MSZ (Fig. S8; see Data and Resources), perhaps suggesting a systemic rupture pattern. The inverted seismic moment (M_0) is 1.46×10^{20} N · m, equivalent to an M_w 7.4 event. The relationship between M_0 and the source rupture duration (τ) satisfies the linear regression analysis $\log(\tau) = (-5.948 \pm 0.236) + (0.362 \pm 0.013)\log(M_0)$, reported by Cruz *et al.* (2020) for interplate Mexican earthquakes. Moreover, to calculate the stress drop ($\Delta\sigma$) for the model from the seismic moment, we assume a simple circular plane with a radius (R) of 27 km. The static stress drop can be expressed by $\Delta\sigma = \frac{7M_0}{16R^3}$ (Kanamori and Anderson, 1975). Therefore, $\Delta\sigma$ is estimated to be 3.2 MPa, consistent with the mean value for the interplate earthquakes (Kanamori and Anderson, 1975; Allmann and Shearer, 2009).

Discussions

Rupture prevented by down-dip SSEs

It has been known that the seismogenic width controls the earthquake magnitude (e.g., Weng and Yang, 2017), which has important implications for the evaluation of the seismic hazard and tsunami potential (e.g., Suárez and Sánchez, 1996; Dixon *et al.*, 2014). The 2020 M_w 7.4 La Crucecita earthquake struck the Oaxaca segment of the MSZ, where the slab subducts at a low angle. Previous studies had pointed out that the coupling depths are shallow in the MSZ, resulting in a narrow

seismogenic width of ~60 km (Singh *et al.*, 1981; Tichelaar and Ruff, 1993; Suárez and Sánchez, 1996; Gao and Wang, 2017). It appears that the small down-dip fault width defines the size of the largest earthquakes in this region (Suárez and Sánchez, 1996; Fasola *et al.*, 2019).

GPS records reveal a large number of SSEs occurring in down-dip of the seismic rupture zone in the MSZ (Fig. 1; Correa-Mora *et al.*, 2009; Song *et al.*, 2009; Graham *et al.*, 2014, 2016; Obara and Kato, 2016; Fasola *et al.*, 2019; Cruz-Atienza *et al.*, 2020). In this case, SSEs release most down-dip shear stress during the interseismic period, limiting the coseismic rupture area and earthquake magnitude. It might cause major events in the seismic cycle to be stopped by the same boundary and produce identical magnitude, resulting in a series of characteristic earthquakes. Singh *et al.* (1981) and Suárez and Sánchez (1996) proposed that large events in this segment of the MSZ have a characteristic magnitude of ~7.5 and an average recurrence interval of 30–50 yr. However, this cannot rule out the possibility that several adjacent faults may rupture together in a single earthquake with much larger magnitude.

Many studies reported that the down-dip boundary of the seismogenic zone in southern Mexico is ~25 km (Tichelaar and Ruff, 1993; Pardo and Suárez, 1995; Suárez and Sánchez, 1996; Gao and Wang, 2017). Our preferred model for the La Crucecita earthquake shows that most slip concentrates between 17 and 24 km. Although, there is limited overlap between our rupture zone and the SSEs identified in previous work, there is very little slip through the 25 km depth (Fig. 1). It is, thus, plausible that SSEs are responsible for the down-dip end of the seismogenic zone, hindering the coseismic down-dip rupture. A similar phenomenon was also observed in the 2012 M_w 7.6 Nicoya earthquake (Dixon *et al.*, 2014). Moreover, a few SSEs are found on the shallower side of the coseismic high-slip region (Correa-Mora *et al.*, 2008; Cruz-Atienza *et al.*, 2020). This may be one of the reasons for the absence of slip in the up-dip zone. The dearth of shallow slip only generates a small tsunami, which could provide important implications for tsunami forecasting in the MSZ. However, the GPS data here are sparse, and the resolution of up-dip SSEs is not high. This still needs further study.

Triggering links between the 2020 M_w 7.4 La Crucecita earthquake and the 2017 M_w 8.2 Chiapas earthquake

Prior to the June 2020 M_w 7.4 La Crucecita earthquake, an M_w 8.2 offshore event occurred in September 2017 about 237 km from the epicenter. Their space–time relationships raise questions about a potential link. We calculate the static coulomb stress change caused by the 2017 Chiapas earthquake, following the strategy of Guo, Zheng, and Xu (2020). In our model, the coseismic driving sources are represented by the finite-fault model (Guo *et al.*, 2019). The specific receiver geometry is the fault location of this 2020 event (strike: 272°, dip: 23°). The effective friction coefficient is set as 0.7, due to the thrust movement of the La Crucecita earthquake. Moreover, our calculations are performed at a depth of 20 km, which is the same as the nucleation depth. The results show that the mainshock of the 2017 Chiapas earthquake increased stress in the source region of the 2020 La Crucecita event (Fig. 4a). However, the coulomb stress change is only ~0.03 bar at the hypocenter of the La Crucecita earthquake (Fig. 4d), lower than the typical triggering threshold of 0.1 bar (e.g., Stein, 1999). Thus, it is unlikely that the coseismic slip of the 2017 Chiapas earthquake had triggered the 2020 La Crucecita earthquake.

After large earthquakes, afterslip can last for several years (e.g., Freed, 2007). Guo *et al.* (2019) estimated the postseismic six-month afterslip distribution for the 2017 Chiapas earthquake and found that the afterslip released a seismic moment equivalent to an M_w 8.0 event. The spatial coverage of aseismic afterslip is much larger than the coseismic rupture zone. The 2020 La Crucecita rupture region is rooted at the eastern extension of the afterslip zone (Fig. S9). We calculate the stress changes caused by the afterslip of the Chiapas earthquake, and find a stress increase between 0.03 and 0.40 bar on the La Crucecita rupture plane (Fig. 4b). It imposes a stress of 0.08 bar at the hypocenter of the 2020 event, accelerating its rupture. The combined effects from the coseismic slip and postseismic afterslip of the 2017 Chiapas earthquake can lead to stress increases of more than 0.1 bar, at the hypocenter of the La Crucecita event (Fig. 4c,d), potentially contributing to the final occurrence of the 2020 event. However, the most important triggering link with the 2020 La Crucecita earthquake comes from the postseismic afterslip of the 2017 Chiapas earthquake, rather than its mainshock.

Using the same source parameters of target fault as earlier, we calculate the expected stress redistribution from the 2020 La Crucecita earthquake at a regional scale. A comparison between the coseismic stress change and the location of aftershocks suggests that postseismic seismicity may be triggered by the mainshock (Fig. S10).

Conclusions

The slip model of the 2020 M_w 7.4 La Crucecita earthquake is well constrained in a narrow asperity between 15 and 25 km. The high-slip region concentrates near the hypocenter location, with a peak magnitude of 5.8 m. There is no significant slip at depths shallower than ~15 km, resulting in a small tsunami. It ruptures bilaterally along strike and is hindered by the down-dip SSEs. The 2017 M_w 8.2 Chiapas earthquake, especially the postseismic afterslip, greatly promotes the occurrence of this event.

Data and Resources

All data in this article are available. Telesesimic body waveforms are downloaded from the Incorporated Research Institutions for Seismology (IRIS) Data Management Center (http://ds.iris.edu/wilber3/find_event, last accessed August 2020). Static Global Positioning System

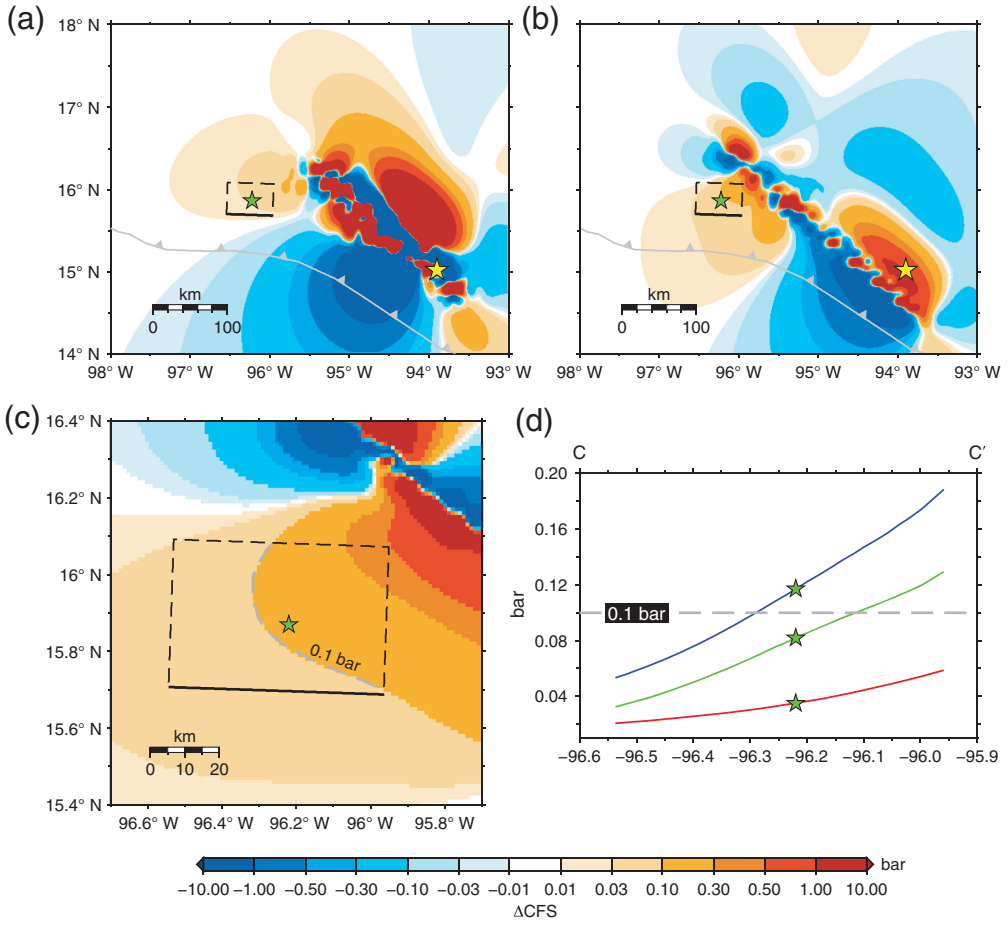

Figure 4. Stress change following the 2017 M_w 8.2 Chiapas earthquake. (a) Coseismic, (b) postseismic afterslip, and (c) combined stress change. Green and yellow stars show the epicenters of the 2017 Chiapas event and the 2020 La Crucecita event, respectively. The black rectangle indicates our preferred slip region. The thick solid line represents our receiver fault. Dashed gray curves show the lower threshold for triggering of 0.1 bar (e.g., Stein, 1999). (d) Stress change due to the 2017 Chiapas earthquake along profile C–C′. Red, green, and blue curves represent the stress changes caused by mainshock, afterslip, and combined effects along profile C–C′, respectively. CFS, Coloumb Failure Stress.

(GPS) displacements are obtained from the Nevada Geodetic Laboratory (NGL) (http://geodesy.unr.edu/, last accessed August 2020). The raw data at Deep-ocean Assessment and Reporting of Tsunamis (DART) station are provided by the National Oceanographic and Atmospheric Administration (NOAA) National Data Buoy Center (https://www.ndbc.noaa.gov/dart.shtml, last accessed August 2020). Tide gauge data are obtained from the website of Intergovernmental Oceanographic Commission (IOC; http://www.ioc-sealevelmonitoring.org/, last accessed August 2020). The bathymetric datasets are from General Bathymetric Chart of the Oceans (GEBCO) (https://www.gebco.net/, last accessed August 2020). The aftershock sequences are from the Servicio Sismológico Nacional (SSN) catalog (http://www.ssn.unam.mx/, last accessed November 2020). The moment rate functions for the 2012 M_w 7.5 Ometepec earthquake and the 2018 M_w 7.2 Pinotepa earthquake are from the U.S. Geological Survey (USGS) (https://earthquake.usgs.gov/). The hypocenters are from the GEOFON (http://geofon.gfz-potsdam.de/eqinfo/event.php?id=gfz2020mhce, last accessed August 2020), Japan Meteorological Agency (http://www.data.jma.go.jp/svd/eqev/data/mech/world_cmt/fig/cmt20200623152905.html, last accessed August 2020), USGS National Earthquake Information Center (NEIC; https://earthquake.usgs.gov/, last accessed August 2020), and the SSN (http://www.ssn.unam.mx/, last accessed November 2020). The supplemental material for this article provides additional 10 figures to support the discussions.

Acknowledgments

The authors thank Editor Allison Bent and two anonymous reviewers for comments that have improved this article. Work for this article is supported by the Chinese Academy of Sciences B-type Strategic Priority Program (Number XDB41000000), National Key R&D Program of China (2018YFC1503400), China Earthquake Science Experiment Project, China Earthquake Administration (CEA; Grant Numbers 2017CESE0101, 2017CESE0103, 2018CSES0101, 2018CSES0102, and 2019CSES0107), the Hong Kong Research Grants Council (Grant Numbers 14313816, 14306418, and 14306119), the Central Universities, China University of Geosciences (Wuhan) Fundamental Research Funds (CUGCJ1707 and 162301132637), and the National Natural Science Foundation of China (NSFC) (Grant Numbers 41874053 and 41874094). All figures are made by the Generic Mapping Tools software (Wessel and Smith, 1991).

References

Allmann, B. P., and P. M. Shearer (2009). Global variations of stress drop for moderate to large earthquakes, *J. Geophys. Res.* **114,** no. B1, doi: 10.1029/2008JB005821.

An, C., I. Sepúlveda, and P. L.-F. Liu (2014). Tsunami source and its validation of the 2014 Iquique, Chile, earthquake, *Geophys. Res. Lett.* **41,** no. 11, 3988–3994, doi: 10.1002/2014GL060567.

Blewitt, G., W. C. Hammond, and C. Kreemer (2018). Harnessing the GPS data explosion for interdisciplinary science, *Eos* **99,** 1–2, doi: 10.1029/2018EO104623.

Chael, E. P., and G. S. Stewart (1982). Recent large earthquakes along the Middle American trench and their implications for the

subduction process, *J. Geophys. Res.* **87,** no. B1, 329–338, doi: 10.1029/JB087iB01p00329.

Chu, R., S. Wei, D. V. Helmberger, Z. Zhan, L. Zhu, and H. Kanamori (2011). Initiation of the great M_w 9.0 Tohoku–Oki earthquake, *Earth Planet. Sci. Lett.* **308,** no. 3, 277–283, doi: 10.1016/j.epsl.2011.06.031.

Correa-Mora, F., C. DeMets, E. Cabral-Cano, O. Diaz-Molina, and B. Marquez-Azua (2009). Transient deformation in southern Mexico in 2006 and 2007: Evidence for distinct deep-slip patches beneath Guerrero and Oaxaca, *Geochem., Geophys. Geosys.* **10,** no. 2, doi: 10.1029/2008GC002211.

Correa-Mora, F., C. DeMets, E. Cabral-Cano, B. Marquez-Azua, and O. Diaz-Molina (2008). Interplate coupling and transient slip along the subduction interface beneath Oaxaca, Mexico, *Geophys. J. Int.* **175,** no. 1, 269–290, doi: 10.1111/j.1365-246X.2008.03910.x.

Cruz, J., C. Arredondo, and M. Jaimes (2020). New source duration relationships for Mexican earthquakes: Practical application to stochastic summation methods, *Pure Appl. Geophys.* **177,** 4775–4796, doi: 10.1007/s00024-020-02552-7.

Cruz-Atienza, V. M., J. Tago, C. Villafuerte, M. Wei, R. Garza-Girón, L. A. Dominguez, V. Kostoglodov, T. Nishimura, S. Franco, J. Real, *et al.* (2020). Short-term interaction between silent and devastating earthquakes in Mexico, Earth and Space Science Open Archive, available at http://www.essoar.org/doi/10.1002/essoar.10503980.2 (last accessed August 2020).

DeMets, C., R. G. Gordon, and D. F. Argus (2010). Geologically current plate motions, *Geophys. J. Int.* **181,** no. 1, 1–80, doi: 10.1111/j.1365-246X.2009.04491.x.

Dixon, T. H., Y. Jiang, R. Malservisi, R. McCaffrey, N. Voss, M. Protti, and V. Gonzalez (2014). Earthquake and tsunami forecasts: Relation of slow slip events to subsequent earthquake rupture, *Proc. Natl. Acad. Sci. Unit. States Am.* **111,** no. 48, 17,039–17,044, doi: 10.1073/pnas.1412299111.

Fasola, S. L., M. R. Brudzinski, S. G. Holtkamp, S. E. Graham, and E. Cabral-Cano (2019). Earthquake swarms and slow slip on a sliver fault in the Mexican subduction zone, *Proc. Natl. Acad. Sci. Unit. States Am.* **116,** no. 15, 7198–7206, doi: 10.1073/pnas.1814205116.

Freed, A. M. (2007). Afterslip (and only afterslip) following the 2004 Parkfield, California, earthquake, *Geophys. Res. Lett.* **34,** no. 6, doi: 10.1029/2006GL029155.

Gao, X., and K. Wang (2017). Rheological separation of the megathrust seismogenic zone and episodic tremor and slip, 7645, *Nature* **543,** no. 7645, 416–419, doi: 10.1038/nature21389.

Graham, S., C. DeMets, E. Cabral-Cano, V. Kostoglodov, B. Rousset, A. Walpersdorf, N. Cotte, C. Lasserre, R. McCaffrey, and L. Salazar-Tlaczani (2016). Slow slip history for the MEXICO subduction zone: 2005 through 2011, *Pure Appl. Geophys.* **173,** no. 10, 3445–3465, doi: 10.1007/s00024-015-1211-x.

Graham, S. E., C. DeMets, E. Cabral-Cano, V. Kostoglodov, A. Walpersdorf, N. Cotte, M. Brudzinski, R. McCaffrey, and L. Salazar-Tlaczani (2014). GPS constraints on the 2011–2012 Oaxaca slow slip event that preceded the 2012 March 20 Ometepec earthquake, southern Mexico, *Geophys. J. Int.* **197,** no. 3, 1593–1607, doi: 10.1093/gji/ggu019.

Guo, R., Y. Zheng, C. An, J. Xu, Z. Jiang, L. Zhang, M. S. Riaz, J. Xie, K. Dai, and Y. Wen (2020). The 2018 M_w 7.9 offshore Kodiak, Alaska, earthquake: An unusual outer rise strike-slip earthquake, *J. Geophys. Res.* **125,** no. 5, e2019JB019267, doi: 10.1029/2019JB019267.

Guo, R., Y. Zheng, and J. Xu (2020). Stress modulation of the seismic gap between the 2008 M_s 8.0 Wenchuan earthquake and the 2013 M_s 7.0 Lushan earthquake and implications for seismic hazard, *Geophys. J. Int.* **221,** no. 3, 2113–2125, doi: 10.1093/gji/ggaa143.

Guo, R., Y. Zheng, J. Xu, and Z. Jiang (2019). Seismic and aseismic fault slip associated with the 2017 M_w 8.2 Chiapas, Mexico, earthquake sequence, *Seismol. Res. Lett.* **90,** no. 3, 1111–1120, doi: 10.1785/0220180262.

Hartzell, S., P. Liu, and C. Mendoza (1996). The 1994 Northridge, California, earthquake: Investigation of rupture velocity, risetime, and high-frequency radiation, *J. Geophys. Res.* **101,** no. B9, 20,091–20,108, doi: 10.1029/96JB01883.

Hayes, G. P., D. J. Wald, and R. L. Johnson (2012). Slab1.0: A three-dimensional model of global subduction zone geometries, *J. Geophys. Res.* **117,** no. B1, doi: 10.1029/2011JB008524.

Helmberger, D. V. (1974). Generalized ray theory for shear dislocations, *Bull. Seismol. Soc. Am.* **64,** no. 1, 45–64.

Hjörleifsdóttir, V., S. K. Singh, A. Husker, V. Hjörleifsdóttir, S. K. Singh, and A. Husker (2016). Differences in epicentral location of Mexican earthquakes between local and global catalogs: An update, *Geofís. Int.* **55,** no. 1, 79–93.

Hu, C., Y. Wu, C. An, and H. Liu (2020). A numerical study of tsunami generation by horizontal displacement of sloping seafloor, *J. Earthq. Tsunami* **14,** no. 4, 2,050,018, doi: 10.1142/S1793431120500189.

Ji, C., D. J. Wald, and D. V. Helmberger (2002). Source description of the 1999 Hector Mine, California, earthquake, Part I: Wavelet domain inversion theory and resolution analysis, *Bull. Seismol. Soc. Am.* **92,** no. 4, 1192–1207, doi: 10.1785/0120000916.

Kanamori, H., and D. L. Anderson (1975). Theoretical basis of some empirical relations in seismology, *Bull. Seismol. Soc. Am.* **65,** no. 5, 1073–1095.

Kumar, A., S. K. Singh, S. Mitra, K. F. Priestley, and S. Dayal (2017). The 2015 April 25 Gorkha (Nepal) earthquake and its aftershocks: Implications for lateral heterogeneity on the Main Himalayan thrust, *Geophys. J. Int.* **208,** no. 2, 992–1008, doi: 10.1093/gji/ggw438.

Lay, T., and A. Rhode (2019). Evaluating the updip extent of large megathrust ruptures using P_{coda} levels, *Geophys. Res. Lett.* **46,** no. 10, 5198–5206, doi: 10.1029/2019GL082774.

Melgar, D., A. Ruiz-Angulo, X. Pérez-Campos, B. W. Crowell, X. Xu, E. Cabral-Cano, M. R. Brudzinski, and L. Rodriguez-Abreu (2020). Energetic rupture and tsunamigenesis during the 2020 M_w 7.4 La Crucecita, Mexico earthquake, *Seismol. Res. Lett.* doi: 10.1785/0220200272.

Obara, K., and A. Kato (2016). Connecting slow earthquakes to huge earthquakes, *Science* **353,** no. 6296, 253–257, doi: 10.1126/science.aaf1512.

Okada, Y. (1985). Surface deformation due to shear and tensile faults in a half-space, *Bull. Seismol. Soc. Am.* **75,** no. 4, 1135–1154.

Pardo, M., and G. Suárez (1995). Shape of the subducted Rivera and Cocos plates in southern Mexico: Seismic and tectonic implications, *J. Geophys. Res.* **100,** no. B7, 12,357–12,373, doi: 10.1029/95JB00919.

Ramírez-Herrera, M.-T., N. Corona, J. Cerny, R. Castillo-Aja, D. Melgar, M. Lagos, A. Goguitchaichvili, M. L. Machain, M. L. Vazquez-Caamal, M. Ortuño, *et al.* (2020). Sand deposits reveal great earthquakes and tsunamis at Mexican Pacific Coast, 1, *Sci. Rep.* **10,** no. 1, 1–10, doi: 10.1038/s41598-020-68237-2.

Rousset, B., C. Lasserre, N. Cubas, S. Graham, M. Radiguet, C. DeMets, A. Socquet, M. Campillo, V. Kostoglodov, E. Cabral-Cano, *et al.* (2016). Lateral variations of interplate coupling along the Mexican subduction interface: Relationships with long-term morphology and fault zone mechanical properties, *Pure Appl. Geophys.* **173,** no. 10, 3467–3486, doi: 10.1007/s00024-015-1215-6.

Sawires, R., M. A. Santoyo, J. A. Peláez, and R. D. Corona Fernández (2019). An updated and unified earthquake catalog from 1787 to 2018 for seismic hazard assessment studies in Mexico, 1, *Sci. Data* **6,** no. 1, 241, doi: 10.1038/s41597-019-0234-z.

Singh, S. K., L. Astiz, and J. Havskov (1981). Seismic gaps and recurrence periods of large earthquakes along the Mexican subduction zone: A reexamination, *Bull. Seismol. Soc. Am.* **71,** no. 3, 827–843.

Song, T.-R. A., D. V. Helmberger, M. R. Brudzinski, R. W. Clayton, P. Davis, X. Pérez-Campos, and S. K. Singh (2009). Subducting slab ultra-slow velocity layer coincident with silent earthquakes in southern Mexico, *Science* **324,** no. 5926, 502–506, doi: 10.1126/science.1167595.

Stein, R. S. (1999). The role of stress transfer in earthquake occurrence, *Nature* **402,** no. 6762, 605–609, doi: 10.1038/45144.

Suárez, G., and O. Sánchez (1996). Shallow depth of seismogenic coupling in southern Mexico: Implications for the maximum size of earthquakes in the subduction zone, *Phys. Earth Planet. In* **93,** no. 1, 53–61, doi: 10.1016/0031-9201(95)03088-3.

Tanioka, Y., and K. Satake (1996). Tsunami generation by horizontal displacement of ocean bottom, *Geophys. Res. Lett.* **23,** no. 8, 861–864, doi: 10.1029/96GL00736.

Tichelaar, B. W., and L. J. Ruff (1993). Depth of seismic coupling along subduction zones, *J. Geophys. Res.* **98,** no. B2, 2017–2037, doi: 10.1029/92JB02045.

Tracy, K.-C., R. Ian, R. David, M. Khalid, P. David, H. Wael, M. Sebastian, M. Eduardo, A. Carlos, R.-G. Jorge, *et al.* (2020). *StEER—Crucecitas, Mexico M_w 7.4 Earthquake: Preliminary virtual Reconnaissance Report (PVRR)*, DesignSafe-CI, doi: 10.17603/ds2-k2bp-t724.

Universidad Nacional Autónoma de México (UNAM) Seismology Group (2013). Ometepec–Pinotepa Nacional, Mexico earthquake of 20 March 2012 (M_w 7.5): A preliminary report, *Geofís. Int.* **52,** no. 2, 173–196, doi: 10.1016/S0016-7169(13)71471-5.

Wang, R., F. Lorenzo-Martín, and F. Roth (2006). PSGRN/PSCMP—A new code for calculating co- and post-seismic deformation, geoid and gravity changes based on the viscoelastic-gravitational dislocation theory, *Comput. Geosci.* **32,** no. 4, 527–541, doi: 10.1016/j.cageo.2005.08.006.

Wang, X., and P. L.-F. Liu (2007). Numerical simulations of the 2004 Indian Ocean tsunamis–coastal effects, *J. Earthq. Tsunami* **1,** no. 3, 273–297, doi: 10.1142/S179343110700016X.

Weng, H., and H. Yang (2017). Seismogenic width controls aspect ratios of earthquake ruptures, *Geophys. Res. Lett.* **44,** no. 6, 2725–2732, doi: 10.1002/2016GL072168.

Wessel, P., and W. H. F. Smith (1991). Free software helps map and display data, *Eos Trans. AGU* **72,** no. 41, 441–446, doi: 10.1029/90EO00319.

Xie, X., and Z. Yao (1989). A generalized reflection-transmission coefficient matrix method to calculate static displacement field of a dislocation source in a stratified half space, *Chin. J. Geophys.* **32,** 191–205.

Yang, H., S. Yao, B. He, and A. V. Newman (2019). Earthquake rupture dependence on hypocentral location along the Nicoya Peninsula subduction megathrust, *Earth Planet. Sci. Lett.* **520,** 10–17, doi: 10.1016/j.epsl.2019.05.030.

Manuscript received 16 September 2020
Published online 13 January 2021